

Microscopic electronic inhomogeneity in the high- T_c superconductor $\text{Bi}_2\text{Sr}_2\text{CaCu}_2\text{O}_{8+x}$

S. H. Pan*, J. P. O'Neal*, R. L. Badzey*, C. Chamon*, H. Ding†, J. R. Engelbrecht†, Z. Wang†, H. Eisaki‡§, S. Uchida‡, A. K. Gupta||, K.-W. Ng||, E. W. Hudson¶§, K. M. Lang¶ & J. C. Davis¶

* Department of Physics, Boston University, Boston, Massachusetts 02215, USA

† Department of Physics, Boston College, Chestnut Hill, Massachusetts 02467, USA

‡ Department of Superconductivity, University of Tokyo, Yayoi, 2-11-16 Bunkyo-ku, Tokyo 113-8656, Japan

|| Department of Physics and Astronomy, University of Kentucky, Lexington, Kentucky 40506-0055, USA

¶ Department of Physics, University of California, Berkeley, California 94720, USA

The parent compounds of the copper oxide high-transition-temperature (high- T_c) superconductors are unusual insulators (so-called Mott insulators). Superconductivity arises when they are 'doped' away from stoichiometry¹. For the compound $\text{Bi}_2\text{Sr}_2\text{CaCu}_2\text{O}_{8+x}$, doping is achieved by adding extra oxygen atoms, which introduce positive charge carriers ('holes') into the CuO_2 planes where the superconductivity is believed to originate. Aside from providing the charge carriers, the role of the oxygen dopants is not well understood, nor is it clear how the charge carriers are distributed on the planes. Many models of high- T_c superconductivity accordingly assume that the introduced carriers are distributed uniformly, leading to an electronically homogeneous system as in ordinary metals. Here we report the presence of an electronic inhomogeneity in $\text{Bi}_2\text{Sr}_2\text{CaCu}_2\text{O}_{8+x}$ on the basis of observations using scanning tunnelling microscopy and spectroscopy. The inhomogeneity is manifested as spatial variations in both the local density of states spectrum and the superconducting energy gap. These variations are correlated spatially and vary on the surprisingly short length scale of ~ 14 Å. Our analysis suggests that this inhomogeneity is a consequence of proximity to a Mott insulator resulting in poor screening of the charge potentials associated with the oxygen ions left in the BiO plane after doping, and is indicative of the local nature of the superconducting state.

We have carried out extensive low-temperature scanning tunnelling microscopy/spectroscopy (STM/S) studies on optimally doped $\text{Bi}_2\text{Sr}_2\text{CaCu}_2\text{O}_{8+x}$. The technical details of the experiments have been reported previously^{2,3}. Various single crystal samples fabricated with different techniques (directional-flux solidification or floating-zone) have been used to ensure the generality of the observations. Some crystals are nominally pure and some are deliberately doped with a very dilute concentration of impurity atoms (Zn or Ni). We have consistently observed a particular type of electronic inhomogeneity regardless of the differences between the individual crystals. This inhomogeneity is manifested as spatial variations in the local density of states (LDOS) spectrum, in the low-energy spectral weight, and in the magnitude of the superconducting energy gap.

As an example, Fig. 1a presents a topographic image obtained on a pure $\text{Bi}_2\text{Sr}_2\text{CaCu}_2\text{O}_{8+x}$ crystal grown by the flux-solidification method. The image reveals the crystal structure of the BiO plane with atomic resolution accompanied by the well known incom-

mensurate structural modulations. In addition, an inhomogeneous background is also discernible. After removing the contrast associated with the above-mentioned topological structures by Fourier filtering, this inhomogeneous background is clearly visible. Assuming that the tunnelling matrix element has no spatial dependence, the resulting image shown in Fig. 1b can be approximated by a map displaying the variation of the integrated LDOS. With spatially resolved spectroscopy, we find that the local tunnelling spectrum also varies from location to location. We discover that the magnitude of the superconducting gap extracted from the local tunnelling spectrum varies spatially as well, instead of exhibiting the single-valued nominal gap of ~ 40 meV that is usually observed by tunnelling in crystals with optimal oxygen doping^{4,5}. Both the integrated LDOS and the superconducting gap magnitude vary on

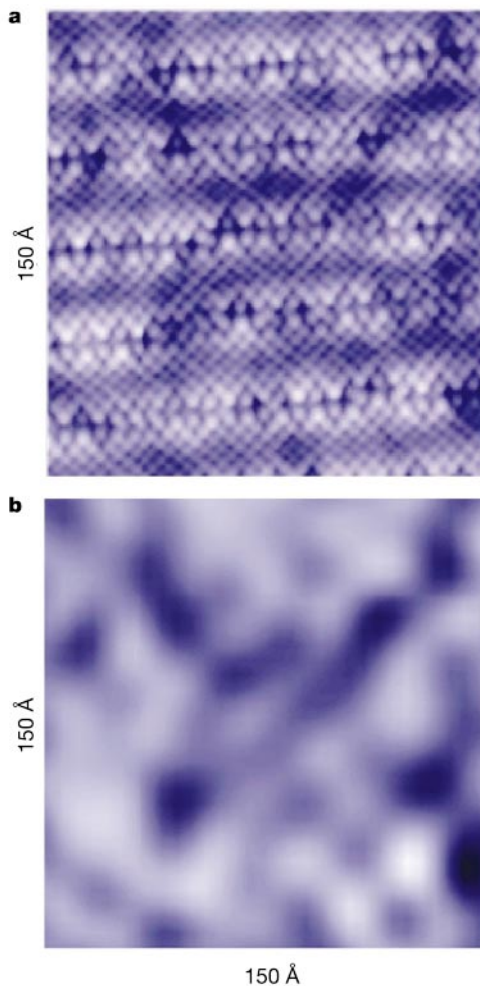


Figure 1 Topographic image and associated integrated LDOS map of an optimally oxygen-doped, nominally pure single crystal of $\text{Bi}_2\text{Sr}_2\text{CaCu}_2\text{O}_{8+x}$. **a**, Constant-current mode, topographic image (150×150 Å) of the surface BiO plane exposed after cleavage of the single crystal. In addition to the clear contrast due to the topological corrugations of the atomic structures and the well known incommensurate structural modulation, an inhomogeneous background is also visible. In constant-current mode, the tunnelling current is exponentially related to the tip-sample distance and is also proportionally related to the integrated LDOS. Therefore, the constant current topographic image provides the convolved information of both the topology and the LDOS of the crystal surface. **b**, To reveal the inhomogeneous background more clearly, we use Fourier filtering to remove the contrast due to the two well-ordered topological structures mentioned above. The variation of the integrated LDOS, which is seen as an inhomogeneous background in **a**, is now clearly displayed. A brighter colour represents a larger magnitude of the integrated LDOS.

§ Present addresses: Department of Applied Physics, Stanford University, Stanford, California 94305, USA (H.E.); and National Institute of Standards and Technology, Gaithersburg, Maryland 20899, USA (E.W.H.).

an apparently much shorter length scale than those in the phenomena observed in earlier experiments^{6,7}. These observations are surprising because in conventional Bardeen–Cooper–Schrieffer (BCS) superconductors (such as Nb) the integrated LDOS, the tunnelling spectrum, and the superconducting gap are spatially homogeneous.

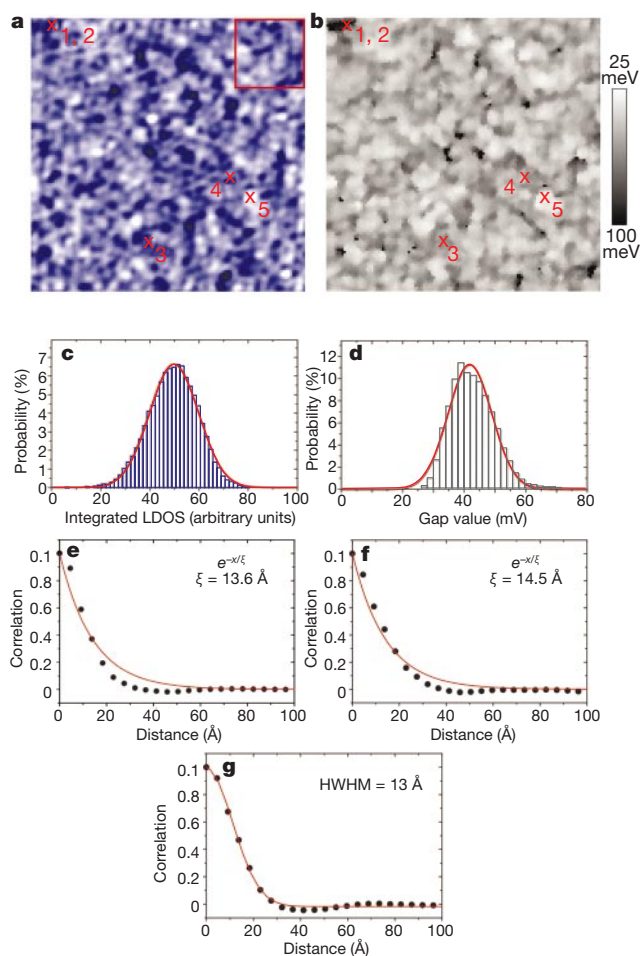


Figure 2 A comparison of an integrated LDOS map and its corresponding superconducting gap map, including their associated statistical results. **a**, A $600 \times 600 \text{ \AA}$ LDOS map obtained with the same technique used in Fig. 1b on a single crystal $\text{Bi}_2\text{Sr}_2\text{CaCu}_2\text{O}_{8+x}$ doped with a very dilute concentration of Zn atoms. (The Zn concentration measured by STM is 0.2%; ref. 2.) The crystal has a superconducting transition temperature of 84 K, with a transition width of 4 K. The red box in panel **a** frames a $150 \times 150 \text{ \AA}$ region for easy comparison with Fig. 1b. It clearly displays an inhomogeneous structure similar to that observed in Zn-free crystals in Fig. 1b. **b**, Superconducting gap map, obtained simultaneously with the integrated LDOS map on the same location, showing the spatial variation of the superconducting energy gap. The local gap values are extracted from the corresponding local differential conductance spectra. We assigned reverse colour coding (higher intensity corresponds to a smaller gap magnitude) to the map so that it is easier to visualize its correlation with the integrated LDOS map. **c** and **d** are the histograms showing the statistical distributions of the integrated LDOS and the magnitude of the superconducting gap. Each of them exhibits a gaussian-like distribution (fitting function displayed in red). The fit of the gap distribution (42 meV mean; $\sim 20 \text{ meV}$ FWHM) shows it to be slightly skewed. **e** and **f** show the azimuthally averaged results of the two-dimensional auto-correlation analysis on the integrated LDOS map and superconducting gap map respectively. Fitting both data sets with a simple exponential decay model (red lines) results in decay lengths of $\sim 14 \text{ \AA}$, demonstrating the short length scale of the variations. The imperfections of the fit imply that a more complex model might be needed. **g**, The superconducting gap is spatially correlated with the LDOS as characterized by this two-dimensional cross-correlation function. It has a pronounced centre peak that can be fitted with a gaussian function.

What is the origin of such an inhomogeneity? Is it intrinsic or caused by impurities such as crystal defects or excess elements that limit the sample quality? Figure 2 is an example of the STM/S results obtained on high quality, floating-zone-grown single crystals deliberately doped with a very dilute concentration (0.2%) of Zn atoms. The inhomogeneous background observed in these crystals (Fig. 2a) is of the same type as that seen in Fig. 1b. This suggests that the inhomogeneity does not originate from impurities. To support this point, we identified the locations of the Zn impurities from a zero bias conductance map, which is taken simultaneously with the LDOS map at the same location³. Using cross-correlation analysis, we found no correlation between the intensity of the integrated LDOS and the locations of the Zn impurities. Furthermore, the length scale of the spatial variation observed in the integrated LDOS map is much smaller than the average impurity spacing. Therefore, we conclude that the inhomogeneity observed in the integrated LDOS is not induced by impurities, but rather is intrinsic in nature.

Spatial variations of the tunnelling spectrum and of the superconducting gap, similar to those observed in the pure sample, are observed in this impurity-doped sample (Fig. 2b). Statistical analysis of Fig. 2a shows that the integrated LDOS has a gaussian distribution, displayed in Fig. 2c. Similarly, analysis of Fig. 2b shows that the gap ranges from 25 meV to 65 meV and exhibits a gaussian distribution (42 meV mean; $\sim 20 \text{ meV}$ full-width at half-maximum, FWHM) as shown in Fig. 2d. We note that the average gap value is very similar to the single value reported on optimally doped $\text{Bi}_2\text{Sr}_2\text{CaCu}_2\text{O}_{8+x}$ in earlier tunnelling measurements^{4,5}.

In addition to the similarity of their statistical distributions, a strong spatial correlation between the integrated LDOS and the superconducting gap can be seen readily by recognizing similar patterns in the two maps (Fig. 2a and b), which are obtained at the same location simultaneously. As illustrated in Fig. 2e–g, auto-correlation analysis on both maps shows similar decay lengths ξ of approximately 14 Å and cross-correlation shows a pronounced gaussian peak, confirming the local nature of the variations and the strong correlation of these two quantities. Furthermore, the line-shape of the local tunnelling spectrum also correlates with the integrated LDOS. As the gap and the integrated LDOS variations are correlated and the energy gap variation cannot be attributed to a tunnelling matrix effect, the inhomogeneity in the integrated LDOS we observe is most probably intrinsic to the electronic structure and not due to a spatially varying matrix element.

Spatial variation of the energy gap and its correlation with the LDOS can be seen in greater detail in Fig. 3. Clearly, the spectra obtained at points with larger integrated LDOS values exhibit higher differential conductance, smaller gap values, and sharper coherence peaks. More significantly, these STM/S results resemble previous tunnelling spectra obtained on samples with different oxygen doping concentrations^{4,5}—the STM/S spectra obtained at positions with higher values of integrated LDOS resemble characteristic spectra obtained on samples with higher oxygen doping concentrations. These observations naturally lead one to relate the magnitude of the integrated local DOS to the local oxygen doping concentration. On a macroscopic scale, such a correspondence is expected for a doped Mott insulator where doping adds spectral weight near the Fermi energy and provides the carriers necessary to transform the insulating compound into a superconductor, as observed previously by photoemission⁸. The idea of local doping concentration (LDC) extends this picture to microscopic scales. In the LDC framework, the charge potentials of oxygen dopants alter the local electronic environment provided that the screening of these potentials is weak on the scale of the inter-carrier distance. For doped Mott insulators, this condition is satisfied by a relatively large inter-carrier distance and strong electronic correlation. A detailed theoretical analysis supporting the LDC framework will be discussed elsewhere.

In Fig. 4, we present a scatter-plot of the magnitude of the energy

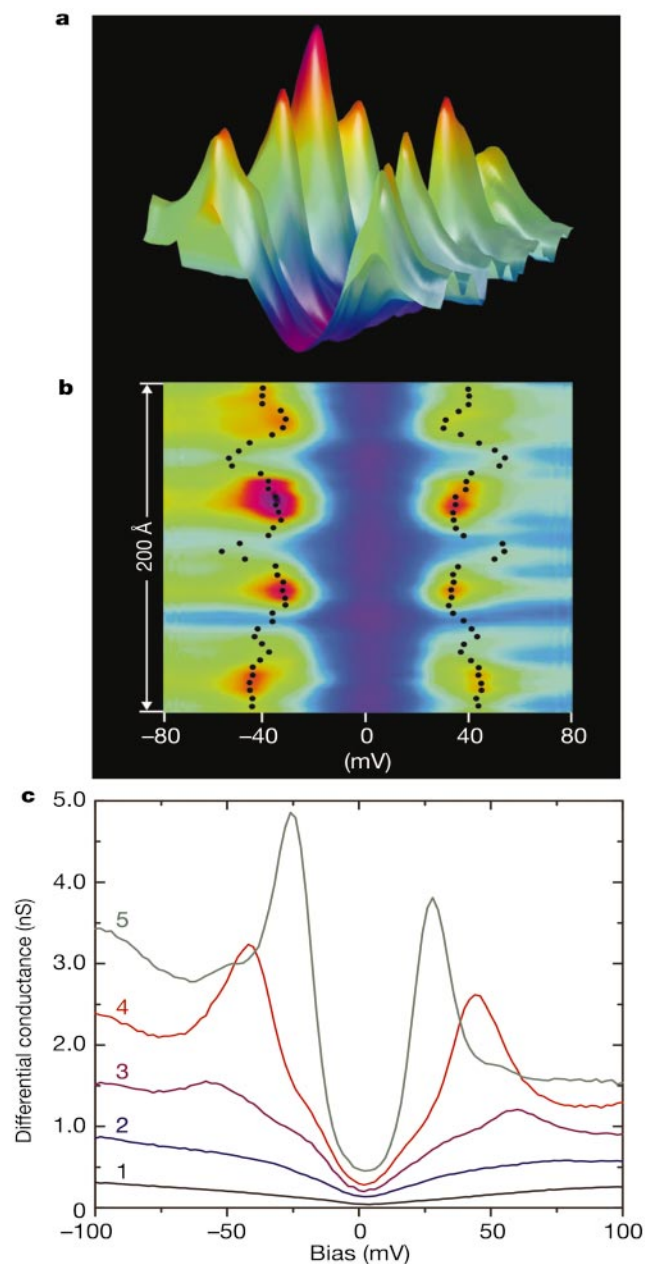


Figure 3 Spatial variation of the tunnelling differential conductance spectrum. To account for variations in the tunnelling junction, the spectra are normalized to a constant tip-sample separation. **a**, A three-dimensional rendering of the tunnelling spectra along a 200 Å line, showing detailed variations of the LDOS, the energy gap, and their correlation. We note that the coherence peak heights vary more dramatically than the gap widths. **b**, The same data as a bird's-eye view. To demonstrate the gap variation, the black dotted lines trace the positions of the coherence peaks. Together with the gap map of Fig. 2b, we can see that the gap varies less rapidly within a 'patch' of high DOS than at its edge. **c**, Five characteristic spectra taken at the positions correspondingly marked in both Fig. 2a and b showing the correlation between the superconducting gap and the integrated LDOS. Curves 1 and 2 are taken at nearby positions in a very dark area on the integrated LDOS map in Fig. 2a, where the integrated LDOS is very small. The low differential conductance and the absence of a superconducting gap are indicative of insulating behaviour. Curve 3 has a large gap of 65 meV, with low coherence peaks, resembling the spectral line-shape measured in oxygen-underdoped samples^{4,5}. The integrated value of the LDOS at the position for curve 3 is small but larger than those in curves 1 and 2, as it is in a slightly brighter area. Curve 4 comes from a still brighter area. It has a gap value of 40 meV, which is close to the mean value of the gap distribution. The coherence peaks are sharper and higher, resembling the spectral behaviour of a sample with optimal oxygen doping^{4,5}. Curve number 5, taken at the position with the highest integrated LDOS, has the smallest gap value of 25 meV with two very sharp coherence peaks, resembling the spectral behaviour of an oxygen over-doped crystal^{4,5}.

gap versus the value of the integrated LDOS. For comparison, the doping dependence of the gap value obtained by angle-resolved photoelectron spectroscopy (ARPES) is superimposed on the plot. We note that STM is a real-space, local probe, whereas ARPES resolves in momentum space but averages in real space over a macroscopic spot. The similarity in the linear behaviour of these two complementary measurements is remarkable, and provides further support for the concept of LDC in this strongly correlated system.

The existence of such microscopic inhomogeneities should have many important consequences on the quasiparticle properties that are accessible by macroscopic measurements. For example, unexpectedly broad peaks in an earlier neutron scattering measurement on $\text{Bi}_2\text{Sr}_2\text{CaCu}_2\text{O}_{8+x}$ could possibly be explained by the presence of inhomogeneity in the bulk⁹. However, it is more important to compare our results to a complementary technique such as ARPES, which measures the same electronic excitations in momentum space under similar experimental conditions. In doing so, we find that taking a spatial average of the STM results yields the same maximum gap value and the same doping dependence of the gap as obtained by ARPES. In addition, the large intrinsic width (~ 20 meV) of the coherence peak measured by ARPES^{10,11} near the antinodes is consistent with the 20 meV FWHM distribution of the superconducting gap shown in Fig. 2d. In light of the electronic disorder observed by this STM experiment, the discrepancy between the nodal and anti-nodal quasiparticle mean free paths observed by ARPES can now be reconciled. Near the antinodes, gap disorder can significantly scatter the quasiparticles at the gap edge. Indeed, the peak in the momentum distribution curve (MDC) near the antinodes has a large width of $\sim 0.08 \text{ \AA}^{-1}$ (ref. 12), corresponding to a short mean free path of $\sim 25 \text{ \AA}$. In the nodal direction, however, ARPES measures a mean free path of $\sim 100 \text{ \AA}$ (refs 13 and 14). The quasiparticles of the *d*-wave superconductor in this direction are less affected by the gap disorder since the latter amounts to velocity disorder in the dispersion, which is not effective at scattering Dirac particles. Thus, the mean free path of the nodal quasiparticles will be

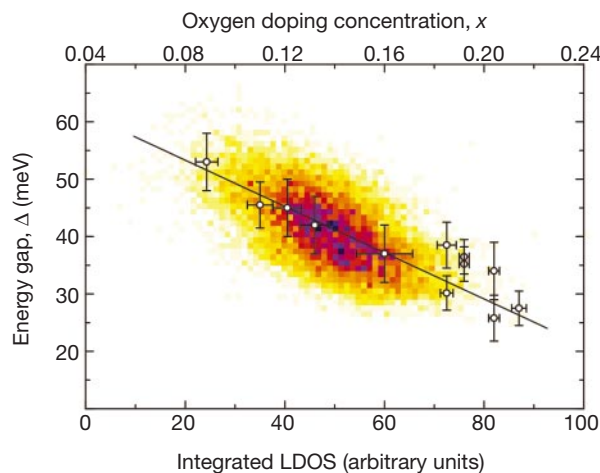


Figure 4 A scatter plot of the superconducting gap versus integrated LDOS. The 16,384 data points of the corresponding integrated LDOS map and the gap map (Fig. 2a, b) are plotted here in colour. A darker colour represents a larger number of data points with the same integrated LDOS and the same gap magnitude. For comparison, a set of data from ARPES measurements on various $\text{Bi}_2\text{Sr}_2\text{CaCu}_2\text{O}_{8+x}$ single crystals with different oxygen doping concentrations is superimposed onto the plot. The gap values of ARPES data are the maximum values of the *d*-wave gap at $(\pi, 0)$ of the Brillouin zone. They are presented as open circles in the plot and the corresponding doping concentration scale is placed on top of the plot. The solid black line is the linear fit to both the STM and the ARPES data.

limited primarily by elastic scattering from the potential disorder. Given that the oxygen dopants responsible for this potential disorder do not reside in the CuO_2 plane, scattering is relatively weak. This can result in a longer mean free path and the measured 100 Å length scale is therefore quite reasonable. As scattering into all angles is involved in ARPES measurements, whereas transport is dominated by large-angle scattering of the nodal quasiparticles, our results may also reconcile the discrepancy between the mean free path measured by transport¹⁵ as compared to that measured by ARPES. Taking 14 Å as the length scale over which the disorder potential varies significantly, we deduce that the dominant elastic scattering process is limited by the wavevector $q = 1/14 \text{ \AA}^{-1}$. The scattering angle, θ , given by $\sin(\theta/2) = q/2k_F$, where k_F is the Fermi wavevector, is indeed quite small at about 5°, which provides a possible explanation as to why the transport mean free path can be much longer than that measured by ARPES.

Discussion of our observations can also be extended to more fundamental issues, such as the coherence of the superconducting state. The coexistence of a high superconducting transition temperature with such a microscopic inhomogeneity implies that the superconducting coherence length is shorter than the mean free path. Our measured gap correlation length, $\xi \approx 14 \text{ \AA}$, sets the length scale for the superconducting pair size in optimally doped $\text{Bi}_2\text{Sr}_2\text{CaCu}_2\text{O}_{8+x}$. By evaluating the BCS expression $\xi_0 = \hbar v_F / \pi \Delta$, taking $\hbar v_F = 1.6 \text{ eV \AA}$ from band dispersion near the nodes^{14,16} and the averaged gap at optimal doping as $\Delta = 0.04 \text{ eV}$, we obtain $\xi_0 \approx 13 \text{ \AA}$, which is in good agreement with the correlation decay length ξ obtained from our experiment. Yet ξ appears to be shorter than the experimental in-plane superconducting coherence length $\xi_{\text{ab}} \approx 22\text{--}27 \text{ \AA}$ (refs 17–19). In contrast to conventional BCS superconductors, it is conceivable that the amplitude and phase coherence in high- T_c superconductors have different length scales, because the ratio $R = 2\Delta/k_B T_c$ is no longer a constant. Recent ARPES measurements¹¹ suggest that $R \propto 1/x$. Thus we may expect the superconducting phase coherence length to be determined by $\hbar v_F / k_B T_c$, which scales as $1/x$ on the underdoped side. An extension of our correlation length and vortex core-size measurements to underdoped samples with various doping concentrations will perhaps distinguish the two length scales because they may have different doping (x) dependences.

The observation of microscopic spatial variations in both the carrier density and the superconducting gap, and the strong correlation between these variations, reveals the local inhomogeneous charge environment in these materials, and its intimate relationship with superconductivity. Further exploration of this frontier may lead to a greater understanding of how high- T_c superconductivity arises from doping a Mott insulator. □

Received 23 January; accepted 18 July 2001.

1. Anderson, P. W. *The Theory of Superconductivity in the High- T_c Cuprates* (Princeton Univ. Press, Princeton, New Jersey, 1997).
2. Hudson, E. W., Pan, S. H., Gupta, A. K., Ng, K.-W. & Davis, J. C. Atomic-scale quasiparticle scattering resonances in $\text{Bi}_2\text{Sr}_2\text{CaCu}_2\text{O}_{8+x}$. *Science* **285**, 88–91 (1999).
3. Pan, S. H. *et al.* Imaging the effects of individual zinc impurity atoms on superconductivity in $\text{Bi}_2\text{Sr}_2\text{CaCu}_2\text{O}_{8+x}$. *Nature* **403**, 746–750 (2000).
4. Renner, Ch. *et al.* Pseudogap precursor of the superconducting gap in under- and overdoped $\text{Bi}_2\text{Sr}_2\text{CaCu}_2\text{O}_{8+x}$. *Phys. Rev. Lett.* **80**, 149–152 (1998).
5. Miyakawa, N. *et al.* Predominantly superconducting origin of large energy gaps in underdoped $\text{Bi}_2\text{Sr}_2\text{CaCu}_2\text{O}_{8+x}$ from tunneling spectroscopy. *Phys. Rev. Lett.* **83**, 1018–1021 (1999).
6. Hasegawa, H., Ikuta, H. & Kitazawa, K. in *Physical Properties of High Temperature Superconductors III* (ed. Ginsberg, D. M.) Ch. 7 (World Scientific, Singapore, 1992).
7. Wolf, E. L., Chang, A., Rong, Z. Y., Ivanchenko, Yu. M. & Lu, F. Direct STM mapping of the superconducting energy gap in single crystal $\text{Bi}_2\text{Sr}_2\text{CaCu}_2\text{O}_{8+x}$. *J. Superconductivity* **70**, 355–360 (1994).
8. Ino, A. *et al.* Doping dependent density of states and pseudogap behavior in $\text{La}_{2-x}\text{Sr}_x\text{CuO}_4$. *Phys. Rev. Lett.* **81**, 2124–2127 (1998).
9. Fong, H. F. *et al.* Neutron scattering from magnetic excitations in $\text{Bi}_2\text{Sr}_2\text{CaCu}_2\text{O}_{8+x}$. *Nature* **398**, 588–591 (1999).
10. Feng, D. L. *et al.* Signature of superfluid density in the single-particle excitation spectrum of $\text{Bi}_2\text{Sr}_2\text{CaCu}_2\text{O}_{8+x}$. *Science* **289**, 277–281 (2000).
11. Ding, H. *et al.* Coherent quasiparticle weight and its connection to high- T_c superconductivity from angle-resolved photoemission. Preprint cond-mat/0006143 at (<http://xxx.lanl.gov>) (2000).

12. Valla, T. *et al.* Temperature dependent scattering rates at the Fermi surface of optimally doped $\text{Bi}_2\text{Sr}_2\text{CaCu}_2\text{O}_{8+x}$. *Phys. Rev. Lett.* **85**, 828–831 (2000).
13. Valla, T. *et al.* Evidence for quantum critical behavior in the optimally doped cuprate $\text{Bi}_2\text{Sr}_2\text{CaCu}_2\text{O}_{8+x}$. *Science* **285**, 2110–2113 (1999).
14. Kaminski, A. *et al.* Quasiparticles in the superconducting state of $\text{Bi}_2\text{Sr}_2\text{CaCu}_2\text{O}_{8+x}$. *Phys. Rev. Lett.* **84**, 1788–1791 (2000).
15. Zhang, Y. *et al.* Giant enhancement of the thermal Hall conductivity κ_{xy} in the superconductor $\text{YBa}_2\text{Cu}_3\text{O}_7$. Preprint cond-mat/0008140 at (<http://xxx.lanl.gov>) (2000).
16. Bogdanov, P. V. *et al.* Evidence for an energy scale for quasiparticle dispersion in $\text{Bi}_2\text{Sr}_2\text{CaCu}_2\text{O}_{8+x}$. *Phys. Rev. Lett.* **85**, 2581–2584 (2000).
17. Palstra, T. T. M. *et al.* Angular dependence of the upper critical field of $\text{Bi}_2\text{Sr}_2\text{CaCu}_2\text{O}_{8+x}$. *Phys. Rev. B* **38**, 5102–5105 (1988).
18. Renner, Ch., Revaz, B., Kadowaki, K., Maggio-Aprile, I. & Fischer, Ø. Observation of the low temperature pseudogap in the vortex cores of $\text{Bi}_2\text{Sr}_2\text{CaCu}_2\text{O}_{8+x}$. *Phys. Rev. Lett.* **80**, 3606–3609 (1998).
19. Pan, S. H. *et al.* STM studies of the electronic structure of vortex cores in $\text{Bi}_2\text{Sr}_2\text{CaCu}_2\text{O}_{8+x}$. *Phys. Rev. Lett.* **85**, 1536–1539 (2000).

Acknowledgements

We acknowledge P. A. Lee and E. W. Plummer for their comments. We also thank P. W. Anderson, A. Balatsky, D. A. Bonn, A. Castro-Neto, E. Carlson, M. Franz, L. H. Greene, X. Hu, T. Imai, B. Keimer, S. A. Kivelson, K. Kitazawa, R. B. Laughlin, D.-H. Lee, A. H. MacDonald, A. Millis, N. P. Ong, Z.-X. Shen, H.-J. Tao, X.-G. Wen, Z.-Y. Weng, N.-C. Yeh, G.-M. Zhang and Z.-X. Zhong for helpful discussions. This work was supported by the NSF, the DOE, the Sloan Research Fellowship, the Research Corporation, the Miller Institute for Basic Research and a Grant-in-Aid for Scientific Research on Priority Area and a COE Grant from the Ministry of Education, Japan.

Correspondence and requests for materials should be addressed to S.H.P. (e-mail: shpan@bu.edu).

.....
Friction and fracture

Eric Gerde & M. Marder

Computational and Applied Mathematics and Center for Nonlinear Dynamics, The University of Texas at Austin, Austin, Texas 78712, USA

.....
Consider a block placed on a table and pushed sideways until it begins to slide. Amontons and Coulomb found that the force required to initiate sliding is proportional to the weight of the block (the constant of proportionality being the static coefficient of friction), but independent of the area of contact. This is commonly explained by asserting that, owing to the presence of asperities on the two surfaces, the actual area in physical contact is much smaller than it seems, and grows in proportion to the applied compressive force. Here we present an alternative picture of the static friction coefficient, which starts with an atomic description of surfaces in contact and then employs a multiscale analysis technique to describe how sliding occurs for large objects. We demonstrate the existence of self-healing cracks^{2–4} that have been postulated to solve geophysical paradoxes about heat generated by earthquakes^{5–11,25–27}, and we show that, when such cracks are present at the atomic scale, they result in solids that slip in accord with Coulomb’s law of friction. We expect that this mechanism for friction will be found to operate at many length scales, and that our approach for connecting atomic and continuum descriptions will enable more realistic first-principles calculations of friction coefficients.

The most intriguing fact about friction is that it is proportional to the force pushing two objects together, but independent of the area of contact. Without contesting the prevalence of materials where the conventional picture involving asperities applies, we wish to point out an alternative way of explaining the same basic fact. Suppose two solids are in close contact over some distance. Suppose further that a wave of separation, a self-healing crack, can run along the interface, like a bump on a rug, leading one solid to slip over the other (Fig. 1). And suppose finally that the condition for such self-